

Accelerated evolution of convective simulations

Evan H. Anders and Benjamin P. Brown

*Dept. Astrophysical & Planetary Sciences, University of Colorado – Boulder, Boulder, CO 80309, USA and
Laboratory for Atmospheric and Space Physics, Boulder, CO 80303, USA*

Jeffrey S. Oishi

Department of Physics and Astronomy, Bates College, Lewiston, ME 04240, USA

We present a method for coupling boundary value problems with initial value problems in order to achieve Accelerated Evolution (AE) of convective solutions on dynamical timescales, rather than the long thermal timescale. We study this method in the context of Rayleigh-Bénard convection. We demonstrate that the solution reached by AE and Standard Evolution (SE) are similar, and that this method works at a large range of supercriticalities. The AE method is used to achieve converged solutions at high supercriticality (10^7), and its extensions to more complex systems are briefly discussed.

I. INTRODUCTION

Natural convection occurs in the presence of disparate timescales which prohibit numericists from studying realistic models of natural systems. For example, flows in the convection zone of stars like the Sun are characteristically low Mach number (Ma) in the deep interior. Explicit timestepping methods which are bound by the Courant-Friedrich-Lewy (CFL) timestep limit must resolve the fastest motions (sound waves), resulting in timesteps which are prohibitively small for studies of the deep, low-Ma motions. These systems are numerically stiff, and the difference between the sound crossing time and the convective overturn time have made studies of low-Ma stellar convection difficult. Traditionally, approximations such as the anelastic approximation, in which sound waves are explicitly filtered out, have been used to study low-Ma flows [1, 2]. More recently, advanced numerical techniques which use implicit or mixed implicit-explicit timestepping mechanisms have made it feasible to study convection at low Mach numbers [3–8], and careful studies of deep convection which would have been impossible a decade ago are now widely accessible.

While solutions to the problem of divergent *dynamical* timescales have proven useful, the difference between convective timescales and thermal timescales, which characterize system relaxation, remain a significant problem facing studies of convection. Solar convection is a prime example of this phenomenon; dynamical timescales in the solar convective zone are relatively short (10 min overturn at solar surface, one month solar rotation rate) compared to the Kelvin-Helmholtz timescale of $3 \cdot 10^7$ years [9]. In such a system, it is impossible to resolve the convective dynamics while also evolving the thermal structure of the system in a meaningful fashion. As modern simulations aim to model natural convection by increasing into the high-Rayleigh-number (Ra) regime, the ratio of the thermal diffusion timescale to dynamical timescales grows [7]. Furthermore, as dynamical and thermal timescales separate, simulations become more turbulent. Increasingly turbulent motions require finer grid meshes and smaller timesteps to capture advective dynamics. Thus, the progression of simulations into the high-Ra regime of natural convection is slowed by two simultaneous effects: timestepping through a single convective overturn time becomes more computationally expensive while the number of overturn times required for systems to reach thermal equilibration grows.

The vast difference between convective and thermal timescales has long plagued numericists studying convection, and an abundance of approaches has been employed to study thermally converged solutions. One popular method for accelerating the convergence of high-Ra solutions is by “bootstrapping” – the process of using the flow fields in a converged solution at lower Ra as initial conditions for a simulation at a higher Ra. This method has been used with great success [10, 11], but it is not without its faults. Bootstrapped solutions are susceptible to hysteresis effects, in which large-scale convective structures present in the low Ra solution imprint onto the dynamics of the new, high Ra solution. Another commonly-used tactic in moderate-Ra simulations is to use a simple model of the full convective state as initial conditions. For example, past studies have used a linear eigenvalue solve to set the initial convective state [12] or used an axisymmetric solution as initial conditions for convection in a 3D cylinder [11]. In certain systems, the approximate state of the evolved solution can be estimated. There, an appropriate set of initial conditions can either be solved for analytically [13] or by using knowledge of Mixing Length Theory or other convective theories to adjust the initial profile towards the proper adiabatic state [14].

Despite the numerous methods that have been used, the most straightforward way to achieve a thermally converged solution is to evolve a convective simulation through a thermal timescale. Some modern studies do just that [2], but it is becoming increasingly difficult. Such evolution is *expensive*, and state-of-the-art simulations at the highest values of Ra can only be reasonably run for tens to hundreds of buoyancy times [15], much less the thousands of buoyancy

timescales required for thermal convergence.

In this work, we study a method of achieving accelerated evolution of a convective simulation through adjusting the thermodynamic state using information from resolved, convective dynamics. We couple measurements of the (non-converged) convective solution with knowledge about energy balances in the eventual solution to self-consistently adjust the mean thermodynamic profile towards its final state. While such a method has been used previously [16], we find no explanation in the current literature of the steps involved in employing this method, nor any study into the accuracy of such a method. In section II, we describe our convective simulations, our numerical methods, and our method for achieving accelerated evolution. In section III, we compare solutions reached through the accelerated evolution method to those that have been evolved through a full diffusive timescale, and we examine select simulations at very high Ra which have achieved accelerated evolution. Finally, in section IV, we discuss extensions of the methods presented here, and we offer concluding remarks in section ??.

II. EXPERIMENT

We study incompressible Rayleigh-Bénard convection under the Oberbeck-Boussinesq approximation, such that our fluid has a constant kinematic viscosity (ν), thermal diffusivity (κ), and coefficient of thermal expansion (α). The density of the fluid is a constant, ρ_0 , except on the term where the constant gravitational acceleration, $\mathbf{g} = -g\hat{z}$, acts in the vertical momentum equation, where $\rho = \rho_0(1 - \alpha T_1)$. Under these constraints, the equations of motion are [17]

$$\nabla \cdot \mathbf{u} = 0, \quad (1)$$

$$\frac{\partial \mathbf{u}}{\partial t} + \mathbf{u} \cdot \nabla \mathbf{u} = -\frac{1}{\rho_0} \nabla P - g(1 - \alpha T_1) \hat{z} + \nu \nabla^2 \mathbf{u}, \quad (2)$$

$$\frac{\partial T_1}{\partial t} + \mathbf{u} \cdot \nabla (T_0 + T_1) = \kappa \nabla^2 T_1, \quad (3)$$

where $\mathbf{u} = u\hat{x} + v\hat{y} + w\hat{z}$ is the velocity, $T = T_0 + T_1$ are the initial and fluctuating components of temperature, and P is the pressure. We non-dimensionalize these equations such that the dimensionless unit of length is the layer height (L_z), temperature is in units of the initial temperature jump across the layer ($\Delta T_0 = L_z \nabla T_0$), and velocity is in units of the freefall velocity ($v_{ff} = \sqrt{\alpha g L_z^2 \nabla T_0}$). by these choices, one time unit is a freefall time (L_z/v_{ff}). We introduce a reduced kinematic pressure, $\varpi \equiv P/\rho_0 + \phi + |\mathbf{u}|^2/2$, where the gravitational potential, ϕ , is defined such that $\mathbf{g} = -\nabla \phi$. As P is a Lagrange multiplier under the Oberbeck-Boussinesq approximation, ϖ can be treated straightforwardly as a linear variable. In non-dimensional form, Eqns. 2 & 3 become

$$\frac{\partial \mathbf{u}}{\partial t} + \nabla \varpi - T_1 \hat{z} + \mathcal{R} \nabla \times \boldsymbol{\omega} = \mathbf{u} \times \boldsymbol{\omega}, \quad (4)$$

$$\frac{\partial T_1}{\partial t} - \mathcal{P} \nabla^2 T_1 + w \frac{\partial T_0}{\partial z} = -\mathbf{u} \cdot \nabla T_1. \quad (5)$$

where $\boldsymbol{\omega} = \nabla \times \mathbf{u}$ is the vorticity. The dimensionless control parameters \mathcal{P} and \mathcal{R} are set by the Rayleigh and Prandtl numbers,

$$\mathcal{R} \equiv \sqrt{\frac{\text{Pr}}{\text{Ra}}}, \quad \mathcal{P} \equiv \frac{1}{\sqrt{\text{Pr Ra}}}, \quad \text{Ra} = \frac{g \alpha L_z^4 \nabla T_0}{\nu \kappa} = \frac{(L_z v_{ff})^2}{\nu \kappa}, \quad \text{Pr} = \frac{\nu}{\kappa}. \quad (6)$$

We hold $\text{Pr} = 1$ constant throughout this work, such that $\mathcal{P} = \mathcal{R}$.

We study 2D and 3D convection in which the domain is a cartesian box, whose dimensionless vertical extent is $z \in [-1/2, 1/2]$, and which is horizontally periodic with an extent of $x, y \in [0, \Gamma]$ where $\Gamma = 2$ is the aspect ratio. In the 2D cases, we set $v = \partial_y = 0$. We specify no-slip, impenetrable boundary conditions at both the top and bottom boundary and we use mixed thermal boundary conditions, such that

$$u = v = w = 0 \text{ at } z = \pm 1/2, \quad T_1 = 0 \text{ at } z = +1/2, \quad \frac{\partial T_1}{\partial z} = 0 \text{ at } z = -1/2. \quad (7)$$

For this choice of boundary conditions, the critical value of Ra at which the onset of convection occurs is $\text{Ra}_{\text{crit}} = 1295.78$, and the supercriticality of a run is defined as $S \equiv \text{Ra}/\text{Ra}_{\text{crit}}$. Studies of convection which aim to model astrophysical systems such as stars often employ mixed thermal boundary conditions [12, 18, 19], as we do here; however, our choice of thermal boundary conditions here reflects the fact that the conditions in Eqn. 7 are the simplest to implement in the process of accelerated evolution (see section II A) we study here.

We utilize the Dedalus¹ pseudospectral framework [20] to evolve Eqns. (1), (4), & (5) forward in time using an implicit-explicit (IMEX), third-order, four-step Runge-Kutta timestepping scheme RK443 [21]. The linear terms (on the LHS of the equations) are solved implicitly, while the nonlinear terms (RHS) are explicitly solved. Variables are time-evolved on a dealiased Chebyshev (vertical) and Fourier (horizontal, periodic) domain in which the physical grid dimensions are 3/2 the size of the coefficient grid.

As initial conditions, we fill T_1 with random white noise whose magnitude is $10^{-6}\mathcal{P}$. This ensures that the initial perturbations are much smaller than the evolved convective temperature perturbations, even at large Ra. We filter this noise spectrum in coefficient space, such that only the lower 25% of the coefficients have power.

A. The method of accelerated evolution

Here we describe a method of Accelerated Evolution (AE). We use this method to quickly evolve the thermodynamic state of our solutions. We compare this method to Standard Evolution (SE), in which we naively evolve the atmosphere for one thermal diffusion time, $t_\kappa = \mathcal{P}^{-1}$. As Ra increases, SE solutions become intractable, while the timeframe of convergence for an AE solution remains nearly constant (in units of freefall times). For an example of time saving achieved by using AE, we compare energy traces at $S = 10^5$ from a SE run in Fig 1a to an AE run in Fig. 1b.

The horizontally averaged profiles of the vertical conductive flux, $F_{\text{cond}} = \langle -\kappa \nabla(T_0 + T_1) \rangle_{x,y}$, and the vertical convective flux, $F_{\text{conv}} = \langle w(T_0 + T_1) \rangle_{x,y}$, where $\langle \rangle_{x,y}$ represent a horizontal average, are the basis of the AE method. We measure both of these quantities early in a simulation, as in Fig. 1c. At these early stages in the simulation, these flux profiles are highly asymmetric, with much more flux leaving through the upper boundary than entering through the lower boundary as the atmosphere approaches the proper isotherm selected by the fixed temperature upper boundary condition. However, by calculating the total flux, $F_{\text{tot}} = F_{\text{conv}} + F_{\text{cond}}$, and then calculating the profiles

$$f_{\text{conv}}(z) = \frac{F_{\text{conv}}}{F_{\text{tot}}}, \quad f_{\text{cond}}(z) = \frac{F_{\text{cond}}}{F_{\text{tot}}}, \quad (8)$$

we remove the asymmetry and examine which parts of the atmosphere are dominated by conduction, and which are not. We presume that the early convection occupies roughly the same volume as the evolved convection, and thus that the early thermal boundary layers are roughly the proper width. Where $f_{\text{conv}} = 1$, convection dominates all transport, and where $f_{\text{cond}} = 1$, conduction dominates all transport (in the boundary layers). Under this assumption, the proper evolved atmospheric flux profiles are $F_{\text{conv, ev}} = F_{\text{bot}} \cdot f_{\text{conv}}$ and $F_{\text{cond, ev}} = F_{\text{bot}} \cdot f_{\text{cond}}$, where $F_{\text{bot}} = \mathcal{P}$ is the amount of flux entering the bottom of the atmosphere.

In the evolved, time-stationary state, the horizontal- and time-average of Eqns. (4) and (5), neglecting terms that vanish due to symmetry, are

$$\frac{\partial}{\partial z} \langle \varpi \rangle_{x,y} - \langle T_1 \rangle_{x,y} \hat{z} = \langle \mathbf{u} \times \boldsymbol{\omega} \rangle_{x,y}, \quad (9)$$

$$\frac{\partial}{\partial z} F_{\text{conv, ev}} - \mathcal{P} \frac{\partial^2}{\partial z^2} \langle T_1 \rangle_{x,y} = 0. \quad (10)$$

Convective flows are perturbations around a thermal profile defined by these equations in the proper evolved, statistically stationary state. Furthermore, under the specification of $F_{\text{conv, ev}}$ and $\langle \mathbf{u} \times \boldsymbol{\omega} \rangle_{x,y}$, the mean thermodynamic structure of the system ($\langle \varpi \rangle_{x,y}$, $\langle T_1 \rangle_{x,y}$) is fully specified.

The AE method is thus simple: we construct $F_{\text{conv, ev}}$ as described above. Then we calculate a profile, $\xi(z) = F_{\text{conv, ev}}/F_{\text{conv}}$, which is the amount that the flux in the system needs to be reduced by, as a function of height. We multiply the velocities and the thermal fluctuations, $T - \langle T \rangle$, by $\sqrt{\xi}$, such that the product of all fluctuations (which carry the convective flux) are diminished by a factor of ξ . We solve Eqns. (9-10) with $F_{\text{conv, ev}}$ and $\xi \cdot \langle \mathbf{u} \times \boldsymbol{\omega} \rangle_{x,y}$ for the mean thermodynamic state, and then continue evolving in time. This adjustment of the mean profile and the diminishing of velocities and fluctuations is the AE method, and it can generally be applied tens of buoyancy times after the peak of convective transient. For specifics on the precise implementation of the AE method, we refer the reader to appendix A.

The AE method specified here quickly converges the fluxes within the system to within a few percent of the fluxes in a system converged through SE (Fig. 1d & e).

¹ <http://dedalus-project.org/>

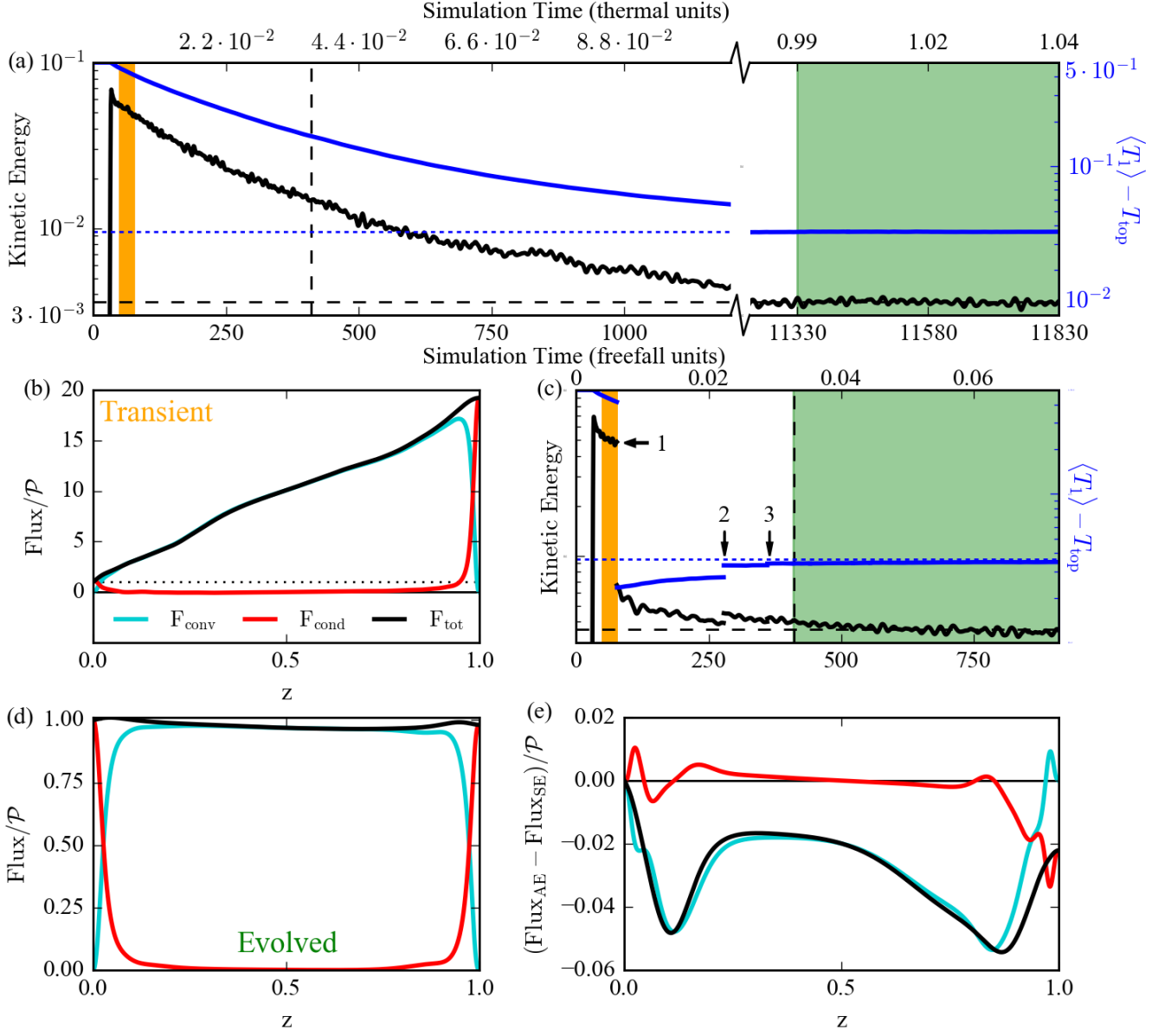


FIG. 1. Traces of kinetic energy and mean temperature vs. time for a (a) SE and (b) AE run are shown at $S = 10^5$. The horizontal extent of the plots is set such that one simulation time unit takes up an equal amount of paper space in (a) and (b). The mean evolved values are shown as horizontal dashed lines. (c) System fluxes shortly after the convective transient are shown, at times corresponding to the orange highlighting in (a) and (b). The sum of the flux is shown in black, the convective flux is shown in purple, and the conductive flux is shown in red. (d) Fluxes in the evolved AE state are shown, measured during the time highlighted in green in (b). (e) The difference between the AE and SE fluxes, measured over the green highlighted regions in (a) and (b), are shown. Note that the black dashed vertical line in (a) denotes the simulation time at which averaging begins for the AE solution shown in (b).

III. RESULTS

We study evolved solutions achieved through the SE method from convective onset up to $S = 10^5$ in 2D and $S = 10^4$ in 3D. These SE runs are compared to AE runs spanning from onset up to $S = 10^7$ in 2D and $S = 10^4$ in 3D. For a full list of simulations, we refer the reader to appendix B.

We report the time- and volume-averaged values of select measurements of the evolved solutions in Fig. 2. We report the scaling of heat transport in the evolved solution, as quantified by the Nusselt number, in Fig. 2a. The

volume averaged Nusselt number is defined as

$$\text{Nu} = \frac{\langle F_{\text{conv}} + F_{\text{cond}} \rangle}{\langle F_{\text{cond, ref}} \rangle} = \frac{\langle wT - \mathcal{P}\partial_z T \rangle}{\langle -\mathcal{P}\partial_z T \rangle}. \quad (11)$$

In 3D and in 2D when $S < 10^{3+2/3}$, the evolved system is defined by a clear value of Nu and the convection reaches a statistically stationary state. In 2D and at larger values of S , the value of Nu oscillates as a function of time as the plumes in the solution oscillate horizontally. Our choice of no-slip boundary conditions prevent the fluid from entering a full-fledged shearing state [22], but the oscillatory motions which do arise cause the system to vary between periods of low heat transport and high heat transport. The SE simulations which span up to $S = 10^5$ exhibit the same horizontally oscillatory motion as the AE solutions for the same initial conditions. The scaling of the mean value of Nu is roughly $\text{Nu} \propto \text{Ra}^{1/5}$, weaker than that reported in similar systems with fixed-T and fixed-flux boundary conditions [10]. We attribute this weaker Nu scaling to the oscillatory nature of the plumes, which may have been avoided by previous studies using bootstrapping techniques as initial conditions.

In Fig. 2b, we report the rms Reynolds number in the AE solutions, where $\text{Re} = \langle |\mathbf{u}| \rangle / \mathcal{R}$. This measure scales roughly as $\text{Re} \propto \text{Ra}^{0.45}$, and shows little variance with time.

In Fig. 2c, we report the volume averaged temperature of the AE solutions, with the value at the upper (fixed T) boundary removed. This measurement probes the thickness of the boundary layers of the solutions, and should show scaling which is inversely proportional to Nu in converged solutions where fixed-flux boundary conditions are used [23]. We find here that $(\langle T \rangle - T_{\text{top}}) \propto \text{Ra}^{-1/5}$, precisely the inverse scaling of Nu, giving confidence that these solutions are in a converged state.

In Fig. 2d-f, we report the fractional difference between measurements from the AE solutions and measurements from the SE solutions. We find that the mean value of Nu from AE solutions is accurate to the values from SE solutions to within $\sim 1\%$, and the same is true for $\langle T \rangle$ measurements. Re measurements show slightly greater error, with AE measurements being on average $\leq 2\%$ away from the SE measurements.

The measurements presented in Fig. 2 demonstrate that the AE method can be powerfully employed in parameter space studies in which large numbers of simulations are compared in a volume-averaged sense. We now turn our examination to a more direct comparison of AE and SE for convection at $S = 10^5$, as has been introduced in Fig. 1.

As the AE method primarily serves to adjust the thermodynamic structure of the solution, we compare the temperature profile attained by AE and SE in Fig. 3. We see that the boundary layer length scale is nearly identical in the AE and SE solution (Fig. 3a), but that the mean temperature in the interior differs by about 0.5% on average (Fig. 3b). The probability distribution function of point-by-point temperature values are compared in Fig. 3c. We construct this PDF by interpolating our temperature field onto a regular grid, determining the frequency distribution of all T values, and then properly normalizing such that the integral of the PDF is unity. In addition to the difference in mode which can be seen in the mean vertical profile, the SE case has a broader spread of temperature values. This can likely be attributed to the slight overstabilization of the temperature profile obtained by the AE method (as can be seen in Fig. 1a&b). One means of comparing two probability distributions to determine if they are drawn from the same underlying sample is through the use of a Kolmogorov-Smirnov (KS) [24]. In general, a KS test must be conducted on independent, uncorrelated data, which poorly describes the point-by-point values of flow in a fluid simulation. Thus, we will merely use the KS statistic, the maximum difference between the cumulative distribution functions (CDFs) of the two sample distributions, as a numerical method of directly comparing the two PDFs. For the distributions shown in Fig. 3c, we find a KS statistic of 0.185 near the modes, which is large, and implies that these two distributions are different.

In addition to comparing the thermodynamic state achieved by the SE and AE methods, we examine the velocities found in the evolved states. We compute PDFs in the same manner as in Fig. 3c for the vertical velocity (Fig. 4a), horizontal velocity (Fig. 4b), and the nonlinear convective flux (Fig. 4c). We report KS statistics of 0.00615, 0.0349, and 0.0204, respectively. Perhaps unsurprisingly, the nonlinear convective transport between the SE and AE methods are very similar, as is captured in a volume-averaged sense in the Nu measurements of Fig. 2a&d). In general, the velocity boundary conditions (Eqn. 7) more strongly dominate the flow fields for the SE cases than the AE cases in Fig. 4a&c. This suggests that the velocity boundary layers are not yet fully formed in the AE solutions. However, aside from this difference, the two solutions show a similar distribution of realized velocity values.

Despite differences between the SE and AE solutions for the case studied in Figs. 1, 3, & 4, the AE method is still extremely powerful. The first application of the AE method ($t \approx 70$ in Fig. 1b) immediately increases the average time step of our solver by a factor of 2-3. At higher supercriticality ($S = 10^7$), the AE solve immediately boosts the timestep by nearly a factor of 4. Thus, not only does this method evolve the solution into nearly the correct state, but further time evolution (either to achieve precisely the correct thermodynamic state or to take measurements of fluid quantities) happens more efficiently.

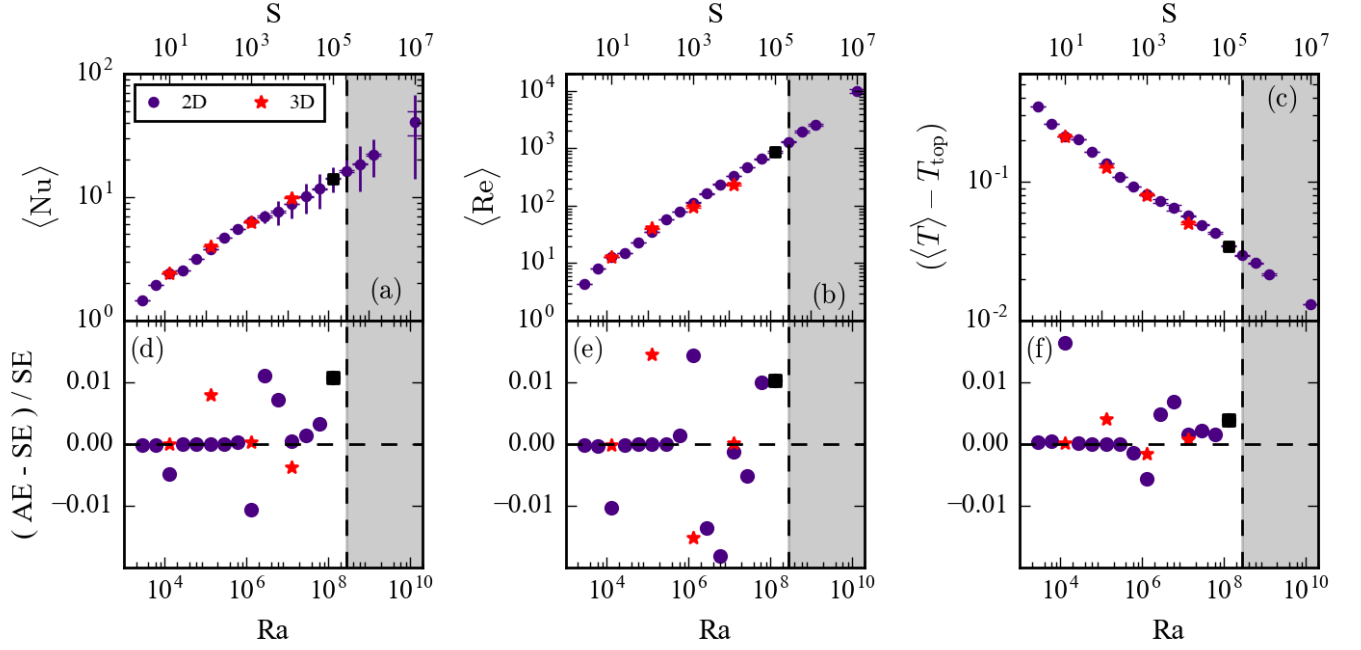


FIG. 2. Volume- and time-averaged measurements for AE runs are shown in (a)-(c). Symbols are located at the mean value of each measurement, while vertical lines represent the standard deviation of the measurement, showing natural variation over the averaging window, and error bars represent the change in the mean value over the window, such that large error bars would represent a poorly converged solution. (a) The Nusselt number scales as $Ra^{1/5}$, and above $S \geq 10^{3+2/3}$, simulations exhibit oscillating plume structures whose heat transport varies over time. (b) The RMS Reynolds number, which measures the level of turbulence in the evolved solution, scales as $Ra^{0.45}$. (c) Temperature, with its value at the upper boundary removed, is shown. Relative error for (d) Nu, (e) Re, and (f) T are shown between measurements taken in AE solutions and SE solutions. The greyed area of the plot indicates the region in which only AE runs were carried out due to computational expense. The run at $S = 10^5$ marked as a black square is examined in more details in Figs. 1, 3, & 4.

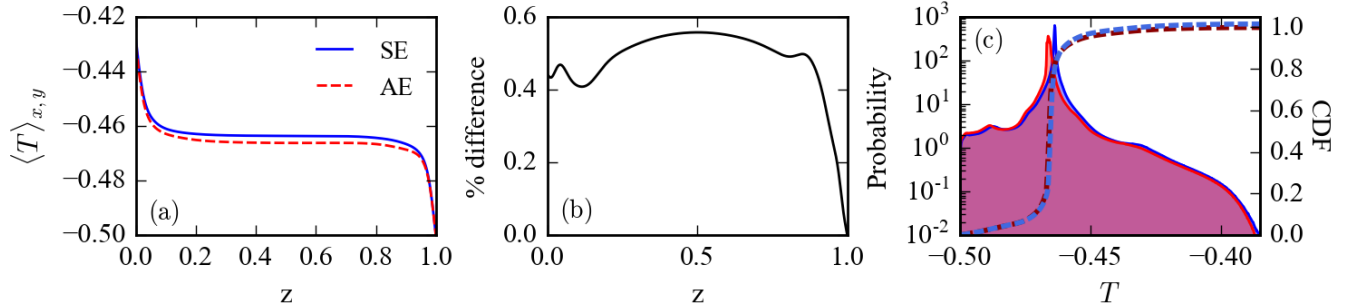


FIG. 3. Comparisons of the evolved thermodynamic states of an AE and SE run at $S = 10^5$ are shown. (a) Evolved temperature profiles, as a function of height. (b) The percentage difference between the temperature profiles as a function of height. (c) Probability distributions of point-by-point measurements of the temperature field. T is sampled every 0.1 time units for 500 total time units, and was interpolated onto an evenly spaced grid before sampling. The cumulative distribution function is overplotted on each plot.

IV. EXTENSIONS & CONCLUSION

In this work we have used Rayleigh-Bénard convection as a test case for the AE method, but we argue that the true power of this method is in its extensions to more complicated studies. Such extensions are beyond the scope of this paper, but we will briefly describe areas in which extensions to the AE method should be explored. We note that a strength of the AE method is its generality. One need only derive the steady-state, horizontally-averaged equations for a given equation set (e.g., Eqns. (9) & (10)) and couple that information with knowledge of the current dynamics

(Eqn. (8)) and the boundary conditions. Thus this method can be easily applied to more complex systems, so long as the experimenter understand the energy transport present in their systems.

In studies of stratified convection where the thermal diffusivity is inversely proportional to the density [7], the thermal timescale deep in the atmosphere is much larger than the timescale near the surface. Thus, the AE method can be a very important tool for studying highly stratified systems which aim to model realistic astrophysical atmospheres. Through carefully examining the flux in excess of the flux conducted along the adiabatic temperature gradient, the fractions of Eqn. (8) can be constructed for such a system. In addition to solving for the average hydrostatic balance and thermal equilibrium, it is essential to simultaneously ensure that mass is conserved in truly stratified systems by adding a mass-conservation equation, similar to those used in stellar structure models [25].

It is common for studies to pair stable and convecting regions [13, 14, 16]. In such studies, particularly when the interface between the stable region and the convecting region is stiff and motions do not penetrate from the convecting region into the stable region, the stable region cannot rely on convective motions to assist in the restratification of the thermal profile. In fully-convective domains, such as those studied here, the atmosphere evolves much more rapidly than the thermal diffusion time (see e.g., Fig. 1a, where the SE solution is essentially fully converged after $4 \cdot 10^3$ frefall units despite the thermal timescale being roughly 10^4 frefall units).

We have only studied solutions in which we use mixed thermal boundary conditions, as in Eqn. 7. However, this method can be easily applied to fixed-temperature boundary conditions, as well. Rather than knowing the total final flux (F_{bot}) through the system a priori, it must be measured using the ratios in Eqn. 8. The integrated conductive flux is known in these systems exactly thanks to the fixed temperature jump across the domain. The total flux through the system (F_{bot}) can be thus $\mathcal{P} / \int f_{\text{cond}} dz$ (double-check). We hesitate to use the AE method for systems in which both boundaries fix the flux, as such systems have degenerate solutions for the temperature.

In conclusion, here we have described a method for converging convective simulations using a method of Accelerated Evolution (AE), and compared it to Standard Evolution (SE) achieved by running simulations for a thermal timescale. We have shown that the AE method produces dynamics that are similar to SE dynamics on much shorter timescales, and have discussed differences that arise between the two methods.

We have shown that the AE method is valid at low values of S , in which solutions converge quickly, and at high values of S , at which SE solutions can take an intractable amount of time. This shows that the AE method not only progresses solutions towards the correct evolved state (at high S), but it also does not throw the simulation out of the correct evolved state (at low S). We have studied the AE method in both 2D and 3D, but since the method relies fundamentally on 1D information from the transient flows, we have restricted most of our study to 2D and merely demonstrated the method's efficacy in 3D, too.

This work serves as a first step towards creating robust methods for achieving evolved convective solutions at high Ra on short timescales. Future studies will extend this method to stratified, fully compressible convection [7], and to systems with internal heating.

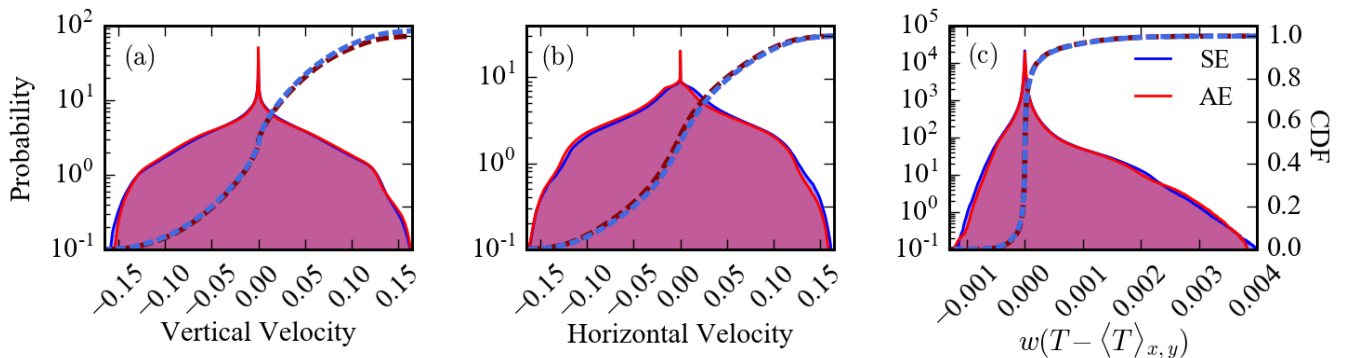


FIG. 4. Probability distribution functions of (a) the vertical velocity, (b) the horizontal velocity, and (c) nonlinear convective transport are shown for a 2D runs achieved through the SE and AE methods at $S = 10^5$. Flows are sampled every 0.1 time units for 500 total time units, and flows are interpolated onto an evenly spaced grid before sampling. The cumulative distribution function is overplotted on each plot.

ACKNOWLEDGMENTS

EHA acknowledges the support of the University of Colorado’s George Ellery Hale Graduate Student Fellowship. This work was additionally supported by NASA LWS grant number NNX16AC92G. Computations were conducted with support by the NASA High End Computing (HEC) Program through the NASA Advanced Supercomputing (NAS) Division at Ames Research Center on Pleiades with allocations GID s1647 and GID g26133.

Appendix A: Accelerated Evolution Recipe

In order to achieve Accelerated Evolution (AE), we solve a 1D Boundary Value Problem consisting of Eqns. (9) & (10). There are a steps required to properly advance the solution are as follows:

1. Update averages of F_{conv} , F_{tot} , and $\langle \mathbf{u} \times \boldsymbol{\omega} \rangle$ every timestep. Wait until that average converges. To ensure that an average is converged, at least some time t_{min} must have passed since the average was started, and the profiles must change by no more than $P\%$ on a given timestep.
2. Construct $F_{\text{conv, ev}}$ and ξ as specified in section II A.
3. Solve for $\langle T_1 \rangle_{x,y}$ and $\langle \varpi \rangle_{x,y}$ of the evolved state. Adjust the profiles in the convecting simulation accordingly
4. Multiply the velocity field and the fluctuations in $T - \langle T \rangle_{x,y}$ by $\sqrt{\xi}$ in the IVP.
5. Continue running the simulation.

We refer to this process as an “AE BVP solve.”

In general, we find that repeating this method multiple times is the best way to ensure that the AE solution is truly converged. For all runs in 2D at $S < 10^5$, we waited for 50 time units after peak transient, completed an AE BVP solve with $t_{\text{min}} = 30$ and $P = 0.1$, waited 50 more time units, and then did a second AE BVP solve with the same parameters. For all 3D runs and 2D runs in the range $S \in [10^5, 10^6]$, we waited 20 time units after peak transient, completed an AE BVP solve with $t_{\text{min}} = 20$ and $P = 1$ in order to quickly reach a near- converged state and vastly increase our timestep. After this, we completed two AE BVP solves, separated by 30 time units each, with $t_{\text{min}} = 30$ and $P = 0.1$ to get very close to the solution (as in Fig. 1b). At very high $S = 10^7$, we ran two AE BVP solves with $t_{\text{min}} = 20$ and $P = 1$, waiting 20 time units after peak transient and 30 time units between the two solves.

Appendix B: Table of Runs

S	Ra	nz	nx, ny	t_{therm}	t_{avg}	Nu _{SE}	Nu _{AE}
$10^{1/3}$	$2.79 \cdot 10^3$	32	64	52.8	100	1.46	1.46
$10^{2/3}$	$6.01 \cdot 10^3$	32	64	77.6	100	1.95	1.95
10^1	$1.30 \cdot 10^4$	32	64	114	100	2.43	2.42
$10^{1+1/3}$	$2.79 \cdot 10^4$	32	64	167	100	2.54	2.54
$10^{1+2/3}$	$6.01 \cdot 10^4$	32	64	245	100	3.14	3.14
10^2	$1.30 \cdot 10^5$	64	128	360	100	3.8	3.8
$10^{2+1/3}$	$2.79 \cdot 10^5$	64	128	528	100	4.71	4.71
$10^{2+2/3}$	$6.01 \cdot 10^5$	64	128	776	100	5.5	5.5
10^3	$1.30 \cdot 10^6$	128	256	$1.14 \cdot 10^3$	200	6.4	6.33
$10^{3+1/3}$	$2.79 \cdot 10^6$	128	256	$1.67 \cdot 10^3$	500	6.87	6.95
$10^{3+2/3}$	$6.01 \cdot 10^6$	256	512	$2.45 \cdot 10^3$	500	7.54	7.59
10^4	$1.30 \cdot 10^7$	256	512	$3.60 \cdot 10^3$	500	8.83	8.83
$10^{4+1/3}$	$2.79 \cdot 10^7$	256	512	$5.28 \cdot 10^3$	500	10.13	10.14
$10^{4+2/3}$	$6.01 \cdot 10^7$	256	512	$7.76 \cdot 10^3$	500	11.65	11.69
10^5	$1.30 \cdot 10^8$	512	1024	$1.14 \cdot 10^4$	500	14.02	14.18
$10^{5+1/3}$	$2.79 \cdot 10^8$	512	1024	$1.67 \cdot 10^4$	500	–	16.21
$10^{5+2/3}$	$6.01 \cdot 10^8$	512	1024	$2.45 \cdot 10^4$	500	–	18.58
10^6	$1.30 \cdot 10^9$	1024	2048	$3.60 \cdot 10^4$	500	–	22.13
10^7	$1.30 \cdot 10^{10}$	2048	4096	$1.14 \cdot 10^5$	200	–	40.78

10^1	$1.30 \cdot 10^4$	32	64×64	114	100	2.42	2.42
10^2	$1.30 \cdot 10^5$	64	128×128	360	100	3.97	4
10^3	$1.30 \cdot 10^6$	128	256×256	$1.14 \cdot 10^3$	500	6.27	6.27
10^4	$1.30 \cdot 10^7$	256	512×512	$3.60 \cdot 10^3$	500	9.92	9.88

- [1] B. P. Brown, M. K. Browning, A. S. Brun, M. S. Miesch, and J. Toomre, “Persistent Magnetic Wreaths in a Rapidly Rotating Sun,” *Astrophys. J.* **711**, 424–438 (2010), [arXiv:1011.2831 \[astro-ph.SR\]](#).
- [2] N. A. Featherstone and B. W. Hindman, “The Spectral Amplitude of Stellar Convection and Its Scaling in the High-Rayleigh-number Regime,” *Astrophys. J.* **818**, 32 (2016), [arXiv:1511.02396 \[astro-ph.SR\]](#).
- [3] M. Viallet, I. Baraffe, and R. Walder, “Towards a new generation of multi-dimensional stellar evolution models: development of an implicit hydrodynamic code,” *Astronomy & Astrophysics* **531**, A86 (2011), [arXiv:1103.1524 \[astro-ph.IM\]](#).
- [4] M. Viallet, I. Baraffe, and R. Walder, “Comparison of different nonlinear solvers for 2D time-implicit stellar hydrodynamics,” *Astronomy & Astrophysics* **555**, A81 (2013), [arXiv:1305.6581 \[astro-ph.SR\]](#).
- [5] M. Viallet, T. Goffrey, I. Baraffe, D. Folini, C. Geroux, M. V. Popov, J. Pratt, and R. Walder, “A Jacobian-free Newton-Krylov method for time-implicit multidimensional hydrodynamics. Physics-based preconditioning for sound waves and thermal diffusion,” *Astronomy & Astrophysics* **586**, A153 (2016), [arXiv:1512.03662 \[astro-ph.IM\]](#).
- [6] D. Lecoanet, B. P. Brown, E. G. Zweibel, K. J. Burns, J. S. Oishi, and G. M. Vasil, “Conduction in Low Mach Number Flows. I. Linear and Weakly Nonlinear Regimes,” *Astrophys. J.* **797**, 94 (2014), [arXiv:1410.5424 \[astro-ph.SR\]](#).
- [7] E. H. Anders and B. P. Brown, “Convective heat transport in stratified atmospheres at low and high Mach number,” *Physical Review Fluids* **2**, 083501 (2017), [arXiv:1611.06580 \[physics.flu-dyn\]](#).
- [8] B. Bordwell, B. P. Brown, and J. S. Oishi, “Convective Dynamics and Disequilibrium Chemistry in the Atmospheres of Giant Planets and Brown Dwarfs,” *Astrophys. J.* **854**, 8 (2018), [arXiv:1802.03026 \[astro-ph.EP\]](#).
- [9] M. Stix, “On the time scale of energy transport in the sun,” *Solar Physics* **212**, 3–6 (2003).
- [10] H. Johnston and C. R. Doering, “Comparison of Turbulent Thermal Convection between Conditions of Constant Temperature and Constant Flux,” *Phys. Rev. Lett.* **102**, 064501 (2009), [arXiv:0811.0401 \[physics.flu-dyn\]](#).
- [11] R. Verzicco and R. Camussi, “Transitional regimes of low-Prandtl thermal convection in a cylindrical cell,” *Physics of Fluids* **9**, 1287–1295 (1997).
- [12] N. E. Hurlburt, J. Toomre, and J. M. Massaguer, “Two-dimensional compressible convection extending over multiple scale heights,” *Astrophys. J.* **282**, 557–573 (1984).
- [13] L.-A. Couston, D. Lecoanet, B. Favier, and M. Le Bars, “Dynamics of mixed convective-stably-stratified fluids,” *Physical Review Fluids* **2**, 094804 (2017), [arXiv:1709.06454 \[physics.flu-dyn\]](#).
- [14] A. Brandenburg, K. L. Chan, Å. Nordlund, and R. F. Stein, “Effect of the radiative background flux in convection,” *Astronomische Nachrichten* **326**, 681–692 (2005), [astro-ph/0508404](#).

- [15] R. J. A. M. Stevens, D. Lohse, and R. Verzicco, “Prandtl and Rayleigh number dependence of heat transport in high Rayleigh number thermal convection,” *Journal of Fluid Mechanics* **688**, 31–43 (2011), [arXiv:1102.2307 \[physics.flu-dyn\]](#).
- [16] N. E. Hurlburt, J. Toomre, and J. M. Massaguer, “Nonlinear compressible convection penetrating into stable layers and producing internal gravity waves,” *Astrophys. J.* **311**, 563–577 (1986).
- [17] E. A. Spiegel and G. Veronis, “On the Boussinesq Approximation for a Compressible Fluid,” *Astrophys. J.* **131**, 442 (1960).
- [18] F. Cattaneo, N. H. Brummell, J. Toomre, A. Malagoli, and N. E. Hurlburt, “Turbulent compressible convection,” *Astrophys. J.* **370**, 282–294 (1991).
- [19] L. Korre, N. Brummell, and P. Garaud, “Weakly non-Boussinesq convection in a gaseous spherical shell,” *Phys. Rev. E* **96**, 033104 (2017), [arXiv:1704.00817 \[physics.flu-dyn\]](#).
- [20] K. Burns, G. Vasil, J. Oishi, D. Lecoanet, and B. Brown, “Dedalus: Flexible framework for spectrally solving differential equations,” *Astrophysics Source Code Library* (2016), [ascl:1603.015](#).
- [21] U. M. Ascher, S. J. Ruuth, and R. J. Spiteri, “Implicit-explicit Runge-Kutta methods for time-dependent partial differential equations,” *Applied Numerical Mathematics* **25**, 151–167 (1997).
- [22] David Goluskin, Hans Johnston, Glenn R. Flierl, and Edward A. Spiegel, “Convectively driven shear and decreased heatflux,” *J. Fluid Mech.* **759**, 360–385 (2014).
- [23] J. Otero, R. W. Wittenberg, R. A. Worthing, and C. R. Doering, “Bounds on Rayleigh Bénard convection with an imposed heat flux,” *J. Fluid Mech.* **473**, 191–199 (2002).
- [24] J. V. Wall and C. R. Jenkins, *Practical Statistics for Astronomers*, by J. V. Wall , C. R. Jenkins, Cambridge, UK: Cambridge University Press, 2012 (2012).
- [25] B. Paxton, L. Bildsten, A. Dotter, F. Herwig, P. Lesaffre, and F. Timmes, “Modules for Experiments in Stellar Astrophysics (MESA),” *The Astrophysical Journal Supplement Series* **192**, 3 (2011), [arXiv:1009.1622 \[astro-ph.SR\]](#).